Identifying lithium *K* edge anisotropy in $LiCoO_2$

Jun Kikkawa,[1,*] Teruyasu Mizoguchi,[2] Masao Arai,[1] Takuro Nagai,[1] and Koji Kimoto[1]
[1]*National Institute for Materials Science, Tsukuba 305-0044, Japan*
[2]*Institute of Industrial Science, The University of Tokyo, Tokyo 153–8505, Japan*

(Received 25 April 2018; published 2 August 2018)

Using scattering-vector ($\boldsymbol{q}$)-dependent electron-energy-loss spectroscopy (EELS), we found anisotropy of Li $1s \rightarrow 2p$ excitation for $LiCoO_2$. To achieve this, EELS spectra for $LiCoO_2$ (i.e., Li *K* edge overlapped with Co $M_{2,3}$ edge) were compared with those of Co $M_{2,3}$ edge for $Na_{0.72}CoO_2$ under dipole transition conditions. Then, first-principles calculations of loss functions and the Bethe-Salpeter equation of Li *K* edge were applied for $LiCoO_2$. We also demonstrate that crystallographic orientation-dependent EELS for $LiCoO_2$ reflects the anisotropy of Li $1s \rightarrow 2p$ excitation.

DOI: 10.1103/PhysRevB.98.075103

I. INTRODUCTION

Identification of anisotropy in an electronic structure and electron excitation is an important subject in widely diverse research fields. For lithium ion batteries, elucidating the anisotropy of physical and electrochemical properties of electrode materials is crucially important for controlling and enhancing Li ion and electron conduction. A fundamentally important electrode material, $LiCoO_2$ [1], has a uniaxial layered structure, implying the presence of anisotropy in electronic structure and conduction of electrons and Li ions. By probing the anisotropy of Co $3d$ and O $2p$ orbitals in Li_xCoO_2, x-ray absorption spectroscopy revealed that holes with strong O $2p$ and itinerant characters play a fundamentally important role in the electronic conductivity of CoO_2 layers with Co^{3+}/Co^{4+} mixed valence [2]. Investigating the anisotropic properties at Li (i.e., local electronic structure, atomic site, and spatial distribution) [3–6] is important for elucidating the electrode material degradation mechanism during electrochemical cycling. Probing the Li *K* edge using electron-energy-loss spectroscopy (EELS) in combination with transmission electron microscopy (TEM) is a powerful method for direct observation of the anisotropy for Li. Deeper understanding of the anisotropic profile in Li *K* edge is indispensable for more accurate quantification of the Li contents and for identification of atomic sites of Li. The presence of anisotropy in Li *K* edge for $LiCoO_2$ is expected to be analogous to other *K* edges in graphite [7–9], hexagonal boron nitrides [10,11], and layered chalcogenides [12]. Nevertheless, despite its importance, the anisotropy of electronic structure at Li in $LiCoO_2$ has never been identified experimentally because the Li *K* edge in EELS overlaps the Co $M_{2,3}$ edge completely.

We overcome this issue by probing the profiles and anisotropy of the Co $M_{2,3}$ edge with $NaCoO_2$, which has a structure similar to that of $LiCoO_2$. In this paper, we describe our achievement of scattering-vector ($\boldsymbol{q}$)-dependent EELS for $LiCoO_2$ and $Na_{0.72}CoO_2$ to clarify the anisotropy of Li *K* edge (Sec. III A), discriminating the $\boldsymbol{q}$ dependences between Li *K* and Co $M_{2,3}$ edges in combination with first-principles calculations. Because this study specifically examines small $\boldsymbol{q}$ suppressing $1s \rightarrow 2s$ excitations, the $\boldsymbol{q}$ dependence of Li *K* edge reflects the anisotropy of $1s \rightarrow 2p$ excitations, i.e., anisotropy of $2p$ states according to the spherical symmetry of the $1s$ state. This point differs from earlier $\boldsymbol{q}$-dependence studies with larger $\boldsymbol{q}$ on Li metal and compounds by inelastic x-ray scattering, reflecting differences between unoccupied $2s$ and $2p$ states [13,14]. Section III B presents an investigation of anisotropy in the loss function, which includes polarization effects (real part of the dielectric tensor) in addition to Li *K* and Co $M_{2,3}$ edges (imaginary part of the dielectric tensor) [15]. For that investigation, first-principles calculations are used with consideration of local-field effects [15–18]. Subsequently, we apply a first-principles Bethe-Salpeter equation (BSE) calculation of the Li *K* edge for consideration of the excitonic interactions [19,20]. Section III C demonstrates that the anisotropy of $1s \rightarrow 2p$ excitations appears in EELS depending on the crystallographic orientation of $LiCoO_2$, as an illustration of practical measurement conditions. Finally, Sec. III D presents discussion of considerations of anisotropy of Li *K* edge for quantifying the Li content in Li_xCoO_2.

II. METHOD

A. EELS experiments

Single-crystalline $LiCoO_2$ and $Na_{0.72}CoO_2$ were prepared using solid-state reactions reported elsewhere [6,21] (see Sec. A in Supplemental Material for structures of $Na_{0.72}CoO_2$ [22]). A monochromated electron microscope (Titan Cubed; FEI Co.) equipped with a spectroscope (Gatan imaging filter, Quantum ERS; Gatan Inc.) was operated with accelerating voltage of 80 kV. Full width at half-maximum of the zero-loss peak in vacuum was 0.15–0.20 eV with energy dispersion of 0.05 eV/ch. Then $\boldsymbol{q}$-dependent EELS (Sec. III A) was conducted with probe size of 30 nm and defocus of 100 μm, i.e., wave-vector resolution of 0.07 nm^{-1} [23], which is approximately equivalent to the effective radius of the circular entrance aperture of the spectroscope on the objective plane.

*kikkawa.jun@nims.go.jp

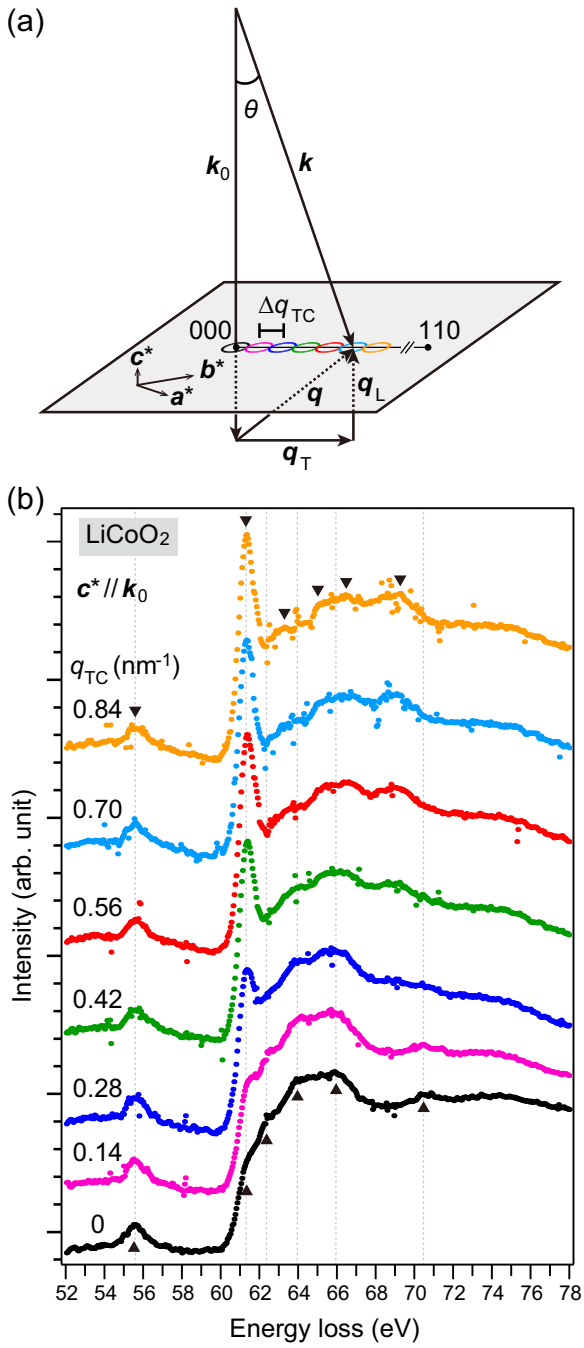

FIG. 1. (a) Scattering diagram in the framework of a two-dimensional detector in EELS. Reduced reciprocal lattice vectors $\boldsymbol{a}^*$, $\boldsymbol{b}^*$, and $\boldsymbol{c}^*$ of $LiCoO_2$ are presented as $\boldsymbol{c}^* \| \boldsymbol{k}_0$. (b) The $\boldsymbol{q}$-dependent EELS spectrum (i.e., superposition of Li K and Co $M_{2,3}$ edges) for $LiCoO_2$, acquired for the [001] electron incident direction from circled areas with radius of $0.070\,\mathrm{nm}^{-1}$ and step increment of $0.14\,\mathrm{nm}^{-1}$.

Figure 1(a) displays a scattering diagram in the framework of a two-dimensional detector in transmission EELS [9,24]. Scattering vector $\boldsymbol{q}$ is defined as $\boldsymbol{q} = \boldsymbol{k}\text{-}\boldsymbol{k}_0$, where $\boldsymbol{k}_0$ and $\boldsymbol{k}$, respectively, represent the incident and scattered wave vectors for primary electrons. They can be decomposed, respectively, into longitudinal (i.e., parallel to $\boldsymbol{k}_0$) and transverse (i.e., perpendicular to $\boldsymbol{k}_0$) components of scattering vectors $\boldsymbol{q}_\mathrm{L}$ and $\boldsymbol{q}_\mathrm{T}$ such that $\boldsymbol{q} = \boldsymbol{q}_\mathrm{L} + \boldsymbol{q}_\mathrm{T}$. Because $q_\mathrm{L} \simeq k_0\theta_\mathrm{E}$ can be written for small scattering angle (i.e., $q_\mathrm{T} \ll k_0$) and $\theta_\mathrm{E} = \Delta E/2E_0$ in nonrelativistic form [7,24], where E_0 and ΔE, respectively, represent the incident energy and energy loss for primary electron, q_L is determined with E_0 and ΔE: $q_\mathrm{L} = 0.56\,\mathrm{nm}^{-1}$ for $E_0 = 80\,\mathrm{keV}$ and $\Delta E = 60\,\mathrm{eV}$. Actually, $\boldsymbol{q}_\mathrm{T}$ is measured as the position on the reciprocal lattice space of the specimen projected on the detector plane. The reduced reciprocal lattice vectors $\boldsymbol{a}^*$, $\boldsymbol{b}^*$, and $\boldsymbol{c}^*$ of the $LiCoO_2$ (space group: $R\bar{3}m$) are also presented as $\boldsymbol{c}^* \| \boldsymbol{k}_0$ in Fig. 1(a): $\boldsymbol{c}^* \| \boldsymbol{c}$ for $R\bar{3}m$. The EELS signal for specific $\boldsymbol{q}$ is measured by selecting the range of $\boldsymbol{q}_\mathrm{T}$ with an aperture and selecting q_L with an energy dispersion system. The dipole condition for $E_0 = 80\,\mathrm{keV}$ and $\Delta E = 60\,\mathrm{eV}$ is $\theta \ll (\Delta E/E_0)^{1/2} \sim 27\,\mathrm{mrad}$, i.e., $|\boldsymbol{q}_\mathrm{T}| \ll 41\,\mathrm{nm}^{-1}$ [11]. Using a small circular aperture with effective radius of $0.070\,\mathrm{nm}^{-1}$ [23] and shifting its center position, $\boldsymbol{q}_\mathrm{TC}$ (i.e., collecting scattered electrons that satisfy $|\boldsymbol{q}_\mathrm{T}\text{-}\boldsymbol{q}_\mathrm{TC}| < 0.070\,\mathrm{nm}^{-1}$) with the step increment $\Delta q_\mathrm{TC} = 0.14$, we obtained the $\boldsymbol{q}$-dependent EELS spectrum from $LiCoO_2$ and $Na_{0.72}CoO_2$. The $\boldsymbol{q}$-dependent EELS described above is proportional to the loss function of

$$L(\omega, q_\mathrm{TC}) = -u^{-2}\mathrm{Im}(v^2\varepsilon_{xx} + \varepsilon_{zz})^{-1}, \qquad (1)$$

for materials with hexagonal unit cells [25,26], where $z \| \boldsymbol{c}$ in a Cartesian coordinate (i.e., xyz) system, $u = q_\mathrm{L} = 0.56\,\mathrm{nm}^{-1}$, $v = q_\mathrm{TC}/0.56 = 0$, 1/4, 1/2, 3/4, 1, 5/4, and 3/2, and $q_\mathrm{TC} = 0$, 0.14, 0.28, 0.42, 0.56, 0.70, and $0.84\,\mathrm{nm}^{-1}$. In addition, $\varepsilon_{xx}(=\varepsilon_{1,xx}+i\varepsilon_{2,xx})$ and, $\varepsilon_{zz}(=\varepsilon_{1,zz}+i\varepsilon_{2,zz})$, respectively, denote the diagonal components of dielectric tensor perpendicular and parallel to the $\boldsymbol{c}$ (and $\boldsymbol{c}^*$) axis. Also, the $\boldsymbol{q} \approx 0$ approximation is appropriate. The increase in q_TC corresponds to the increase in the contribution of ε_{xx} against ε_{zz} in $L(\omega, q_\mathrm{TC})$, i.e., the EELS spectrum. In Sec. III C, orientation-dependent EELS was applied using diffraction mode with the convergence semiangle of 0.75 mrad (equivalent to $1.1\,\mathrm{nm}^{-1}$) and collection radii of scattered electrons, 7.0 and $3.4\,\mathrm{nm}^{-1}$ [7,26].

B. Theoretical calculations

First-principles calculations of the loss function were conducted using the full potential linear augmented plane-wave (FPLAPW) method with exciting code in the framework of time-dependent density-functional theory with random-phase approximation and a long-wavelength limit [27]. The exchange-correlation energy functional was treated with generalized-gradient approximation (GGA) with the Perdew-Burke-Ernzerhof functional form [28]. Local-field effects [15–18], which are indeed crucially important for Co $M_{2,3}$ edge of $LiCoO_2$ (Sec. B in Supplemental Material [22]) are included in the calculations of loss functions. First-principles BSE calculations of Li K edge were conducted using the FPLAPW method with ELK code [29]. The excitonic interaction (i.e., electron-hole interaction) is known to have strong effects on the Li K edge [19,20]. Therefore, solving the BSE is necessary to ascertain the excitonic effect accurately. The effective two-particle Hamiltonian with spin-orbit interaction, which treats the excitonic effect, is described as $H^\mathrm{eh} = H^\mathrm{diag} + H^\mathrm{dir} + H^x$, where H^diag, H^dir, and H^x, respectively, denote the diagonal, direct, and exchange terms, as reported earlier in the literature

[30,31]. To calculate the BSE, one-particle wave functions obtained from the GGA calculation were used for this study. The BSE-GGA method does not estimate the transition energy correctly. Therefore, the calculated spectra were shifted manually using a particular peak.

III. RESULTS AND DISCUSSION

A. q-dependent EELS

Figure 1(b) shows the $\boldsymbol{q}$-dependent EELS spectrum (i.e., superposition of Li K and Co $M_{2,3}$ edges combined with polarization effects) from $LiCoO_2$ for $\boldsymbol{q}_L \| \boldsymbol{c}^*$, $\boldsymbol{q}_{TC} \| (\boldsymbol{a}^* + \boldsymbol{b}^*)$ after background subtraction by fitting with first-order log-polynomials in the ranges of 5.0 eV between 43 and 49 eV (see Fig. S3(a) for the raw spectrum [22]). For $q_{TC} = 0\,\mathrm{nm}^{-1}$ (i.e., $\boldsymbol{q}$ is approximately parallel to $\boldsymbol{c}^*$), major intensities are found at 55.5, 61.4, 62.5, 63.9, 65.9, and 70.5 eV, as denoted by upward-pointing triangles [▲; Fig. 1(b)]. For $q_{TC} = 0.84\,\mathrm{nm}^{-1}$ (i.e., $\boldsymbol{q}$ has the angle of approximately 57° to $\boldsymbol{c}^*$), major intensities are located at 55.5, 61.4, approximately 63.6, 65.4, 66.5, and approximately 69.0 eV, as denoted by downward-pointing triangles [▼; Fig. 1(b)]. It is noteworthy that the intensity at 61.4 eV depends strongly on q_{TC}. The continuous spectrum variation from $q_{TC} = 0$ to $0.84\,\mathrm{nm}^{-1}$ shows clearly that EELS with $\boldsymbol{q} \| \boldsymbol{c}^*$ differs from EELS with $\boldsymbol{q} \| (\boldsymbol{a}^* + \boldsymbol{b}^*)$. The latter signals become dominant beyond the crossover point: $0.56\,\mathrm{nm}^{-1}$. Because the contribution of ε_{xx} in $L(\omega, q_{TC})$ increases as q_{TC} increases, the spectrum variation in Fig. 1(b) originates from the difference between ε_{xx} and ε_{zz}, i.e., either or both differences in real and imaginary parts. The difference between $\varepsilon_{1,xx}$ and $\varepsilon_{1,zz}$ is related with the anisotropy of polarization effects [15], whereas the difference between $\varepsilon_{2,xx}$ and $\varepsilon_{2,zz}$ is related with the anisotropy of either or both of Li K and Co $M_{2,3}$ edges in the energy range of 52–78 eV.

To discriminate the $\boldsymbol{q}$ dependence of Li K edge from that of Co $M_{2,3}$ edge combined with polarization effects for $LiCoO_2$ [Fig. 1(b)], we applied $\boldsymbol{q}$-dependent EELS for $Na_{0.72}CoO_2$ with $\boldsymbol{c}^* \| \boldsymbol{k}_0$ (Sec. A in Supplemental Material [22] with Ref. [32]), as presented in Fig. 2 after background subtraction by fitting with first-order log-polynomials at ranges of 6.0 eV between 43 and 49 eV [see Fig. S3(b) for the raw spectrum]. The spectrum feature of Co $M_{2,3}$ edge for $Na_{0.72}CoO_2$ is similar to that for $LiCoO_2$ because Co^{4+} ions in $Na_{0.72}CoO_2$ contribute only slightly to increases in intensity and $\boldsymbol{q}$ dependence at 59.4 eV, and to a faint chemical shift (approximately 0.2 eV; see Sec. C in Supplemental Material [22] with Ref. [33]). Assuming that the $\boldsymbol{q}$ dependence of polarization effects for $Na_{0.72}CoO_2$ is similar to that for $LiCoO_2$ in a small range of q_{TC} (i.e., $0 \leqslant q_{TC} < 1\,\mathrm{nm}^{-1}$), we can approximately examine the $\boldsymbol{q}$ dependence EELS without Li K edge for $LiCoO_2$ by probing the $\boldsymbol{q}$ dependence EELS for $Na_{0.72}CoO_2$ at energies of 52–78 eV. The $\boldsymbol{q}$ dependence of Co $M_{2,3}$ edge combined with polarization effects (Fig. 2), where characteristic intensities are denoted, respectively, as solid (■) and open (□) squares for $q_{TC} = 0$ and $0.84\,\mathrm{nm}^{-1}$, is sufficiently small in comparison to the $\boldsymbol{q}$ dependence of the superposition of Li K and Co $M_{2,3}$ edges combined with polarization effects [Fig. 1(b)]. The slight $\boldsymbol{q}$ dependence is that deriving from decreased EELS intensity at 59.4 eV and 64–67 eV relative to the intensity

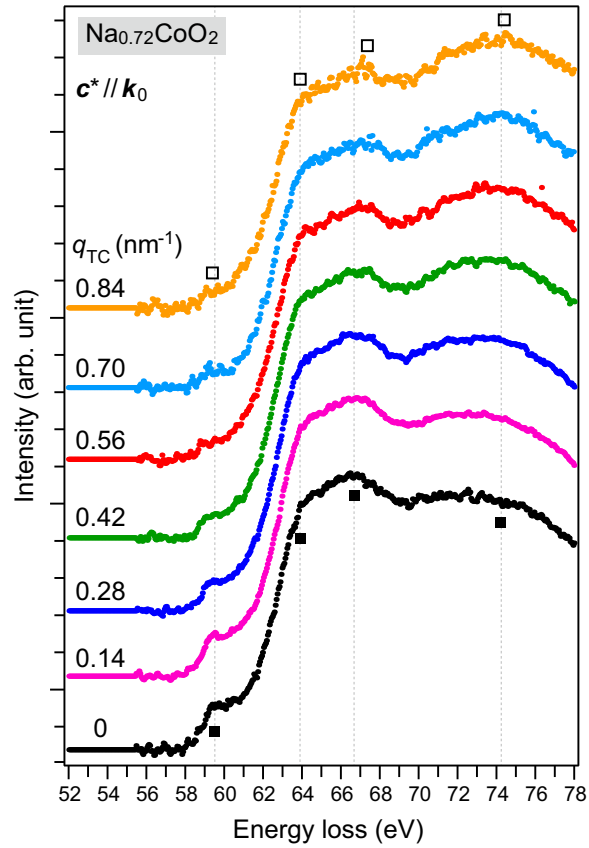

FIG. 2. $\boldsymbol{q}$-dependent Co $M_{2,3}$ edge for $Na_{0.72}CoO_2$ with [001] electron incident direction.

at 70–79 eV and shift of the local maximum at 66.7 eV to the higher energy-loss side, with increased q_{TC} from 0 to $0.84\,\mathrm{nm}^{-1}$. The small $\boldsymbol{q}$ dependence of EELS for $Na_{0.72}CoO_2$ in comparison to that of $LiCoO_2$ is not caused by undesirable subtractions of background intensities because which relation is also confirmed in the raw spectra in Fig. S3. Consequently, the experimentally obtained results signify that the marked variation in EELS intensity at 61.4 eV in Fig. 1(b) originates from the $\boldsymbol{q}$ dependence of the Li K edge.

B. Calculated loss function and Li K edge, compared with experimentally obtained values

Loss functions $L(\omega, q_{TC})$ for $q_{TC} = 0$ and $q_{TC} \gg q_L$ are written as $L(\omega) = L_{zz}(\omega)$ and $L(\omega) \approx L_{xx}(\omega)$, respectively, from Eq. (1). Results of first-principles calculations of $L_{zz}(\omega)$ and $L_{xx}(\omega)$ including local-field effects for $LiCoO_2$ are shown as "full" in Fig. 3: The profiles for full in Figs. 3(a) and 3(b) are identical. For realizing the contributions of Li K and Co $M_{2,3}$ edges in $L(\omega)$, $L(\omega)$ without Li $1s$ and Co $3p$ excitations are displayed, respectively, in Figs. 3(a) and 3(b). In addition, differences between full and $L(\omega)$ without Li $1s$ and Co $3p$ excitations are denoted, respectively, as the dashed lines in Figs. 3(a) and 3(b). The profiles of "difference" in Figs. 3(a) and 3(b) reflect that Li K and Co $M_{2,3}$, respectively, have edges of 46–65 and 63–80 eV. An important point is that the difference between $L_{xx}(\omega)$ and $L_{zz}(\omega)$ without Li $1s$ excitations (green and blue lines, respectively) is small in comparison to that with

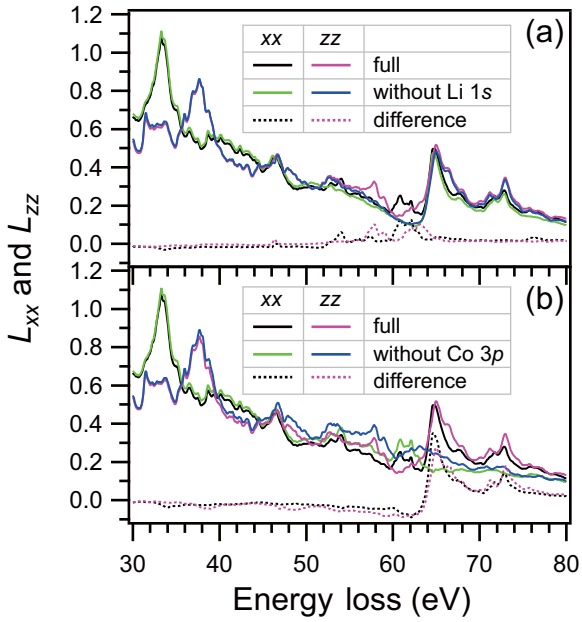

FIG. 3. Calculated loss functions of L_{xx} and L_{zz} (denoted as full), with L_{xx} and L_{zz} excluding excitations of Li 1s in (a) and Co 3p in (b). Differences between full and "without Li 1s/Co 3p" in L_{xx} and L_{zz} are shown as dashed lines.

full excitations (black and magenta lines, respectively) in the energy range of 46 and 80 eV [Fig. 3(a)]. This fact demonstrates that the anisotropy of $L(\omega, q_{\mathrm{TC}})$ for $LiCoO_2$ predominantly originates from the anisotropy of Li K edge rather than from the anisotropy of Co $M_{2,3}$ edge combined with polarization effects (i.e., real part of dielectric tensor). The calculated result is consistent with the experimentally obtained result signifying that the marked variation in EELS intensity at 61.4 eV in Fig. 1(b) originates from the $\boldsymbol{q}$ dependence of the Li K edge.

Because of the spherical symmetry of the 1s state, the $\boldsymbol{q}$ dependence of Li K edge satisfying the dipole approximation signifies the presence of substantial anisotropy of 2p state in the excitation process. Difference between the $2p_x(=2p_y)$ and $2p_z$ states conceivably derives from the perspective of crystallographic symmetry ($R\bar{3}m$), where $z \| c$ in the Cartesian coordinate (i.e., xyz) system. For deeper understanding of the profile of Li K edge, a first-principles BSE calculation of Li K edge is applied. The calculated result illustrates the difference between $2p_{xy}(\equiv 2p_x,\ 2p_y)$ and $2p_z$ states. In Fig. 4, the EELS spectra of $LiCoO_2$ for $q_{\mathrm{TC}} = 0$ and $0.84\,\mathrm{nm}^{-1}$ [Fig. 1(b)] are presented, respectively, for comparison with the spectra of $Na_{0.72}CoO_2$ for $q_{\mathrm{TC}} = 0$ and $0.84\,\mathrm{nm}^{-1}$ (Fig. 2) and the BSE calculations for $1s \rightarrow 2p_z$ and $1s \rightarrow 2p_{xy}$ excitations. There, the calculated profiles are arranged with arbitrary energy shifts for comparison with experimentally obtained results because the present BSE calculation does not provide correct excitation energies. Characteristic intensities in EELS for $LiCoO_2$ are assigned to Li K and Co $M_{2,3}$ edges with solid (•) and open (○) circles for $q_{\mathrm{TC}} = 0$ and solid (■) and open (□) squares for $q_{\mathrm{TC}} = 0.84\,\mathrm{nm}^{-1}$ (Fig. 4). In the EELS spectra for $LiCoO_2$ (Fig. 4), intensities from Co $M_{2,3}$ edges are observable at approximately 75 eV for $q_{\mathrm{TC}} = 0$ and $0.84\,\mathrm{nm}^{-1}$ and at 59.4 eV for $q_{\mathrm{TC}} = 0\,\mathrm{nm}^{-1}$, whereas features in Co $M_{2,3}$ edges

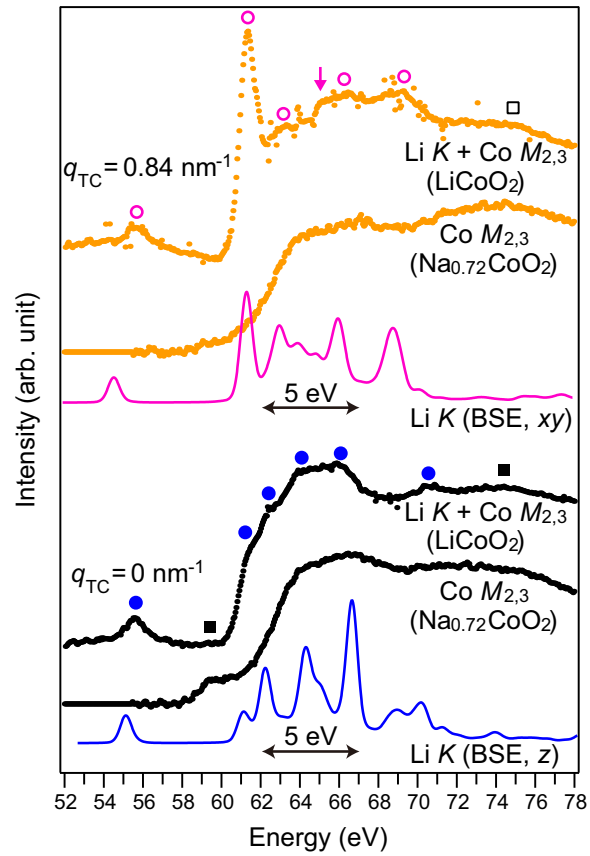

FIG. 4. Comparisons among superpositions of Li K and Co $M_{2,3}$ edges for $LiCoO_2$ [Fig. 1(b)] Co $M_{2,3}$ edge for $Na_{0.72}CoO_2$ (Fig. 2), and calculated Li K edge with the BSE equation. Spectra for $q_{\mathrm{TC}} = 0$ and $0.84\,\mathrm{nm}^{-1}$ are compared, respectively, with xy and z components of the calculated Li K edge.

at 63.7 and 66.7–67.5 eV (Fig. 2) are not explicitly observable, but they exist as fundamentally important components. In Fig. 4, the other fine features (i.e., solid and open circles) in the experimental spectra for $LiCoO_2$ are assigned to signals originated from the Li K edge and which are explainable with the calculated Li K edges for $1s \rightarrow 2p_z$ and $1s \rightarrow 2p_{xy}$ excitations. This explanation supports that $1s \rightarrow 2p_{xy}$ and $1s \rightarrow 2p_z$ excitations, respectively, denote the major and minor components in EELS spectrum for $q_{\mathrm{TC}} = 0.84\,\mathrm{nm}^{-1}$, whereas $1s \rightarrow 2p_z$ excitation dominates the EELS spectrum for $q_{\mathrm{TC}} = 0\,\mathrm{nm}^{-1}$.

C. Orientation-dependent EELS

Because of the presence of anisotropy of Li 2p state for $LiCoO_2$ as clarified above, the EELS signal depends on the crystallographic orientation against the electron incident direction when the range of $\boldsymbol{q}_{\mathrm{T}}$ is fixed. This point was demonstrated with a larger range of $\boldsymbol{q}_{\mathrm{T}}$ (but with dipole transitions still predominant) used in conventional TEM–EELS analyses (Fig. 5). The EELS spectra (i)–(v) [Fig. 5(c)] were acquired from $LiCoO_2$ with electron incident directions of [001], [211], [511], [841], and [100] [Fig. 5(a)] and $|\boldsymbol{q}_{\mathrm{T}}| \leqslant 7.0\,\mathrm{nm}^{-1}$, as denoted by solid circles in Fig. 5(b) for the case of [100]. The angles against the $\boldsymbol{c}$ axis for the [211], [511], [841], and

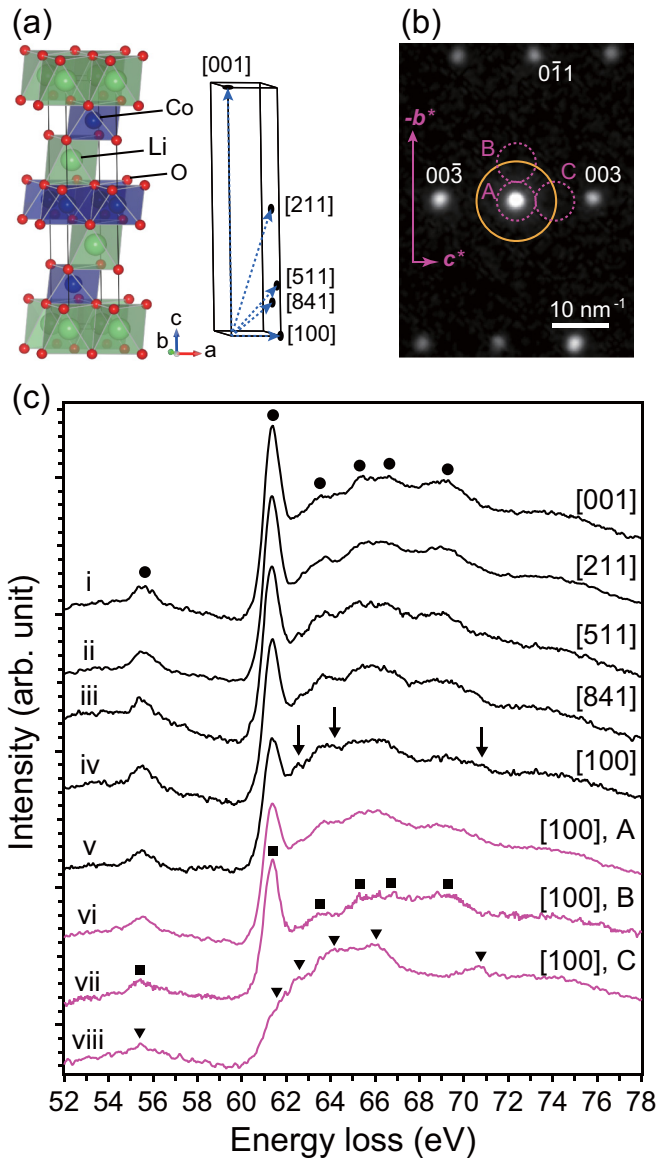

FIG. 5. (a) Drawings of the crystal structure of $LiCoO_2$ and its unit-cell frame with arrows indicating electron incident directions in EELS. (b) [100] electron diffraction pattern. The scale is calibrated with $2\pi/d$, where d is the length in real space. (c) EELS spectra from $LiCoO_2$ acquired using scattered electrons into the solid circle in (b) with different electron incident directions for (i)–(v) and scattered electrons into the dotted circles, A–C in (b) with [100] electron incident direction for (vi)–(viii).

[100] directions are, respectively, 19.1°, 42.5°, 54.2°, and 90° [Fig. 5(a)]. The variation of spectrum features from (i) to (v) in Fig. 5(c) is attributable to the increase in EELS intensity from $1s \rightarrow 2p_z$ excitation relative to that from $1s \rightarrow 2p_{xy}$ excitation. In Fig. 5(c), spectrum (i) for [001] has peaks at 55.5, 61.4, 63.6, 65.4, 66.7, and 69.2 eV (denoted as solid circles), similarly to the spectrum for $q_{TC} = 0.84\,nm^{-1}$ in Fig. 1(b), which mainly reflects $1s \rightarrow 2p_{xy}$ excitation because the EELS signals are integrated up to large $\boldsymbol{q}_T(>0.56\,nm^{-1})$ in the plane parallel to both $\boldsymbol{a}^*$ and $\boldsymbol{b}^*$ (Sec. E in Supplemental Material [22]). Spectrum (v) for [100] has a reduced peak at 61.4 eV and additional intensities at 62.5, 64.2, and 70.8 eV [indicated by arrows in Fig. 5(c)] as a result of the increase in contribution of $1s \rightarrow 2p_z$ excitation. The contribution was confirmed by the detection of inelastic electrons scattered separately in the $-\boldsymbol{b}^*$ and $\boldsymbol{c}^*$ directions, with the detection range of $\boldsymbol{q}_T$ shown as dotted circles, B and C in Fig. 5(b). The ranges of $\boldsymbol{q}_T$ are described as $|\boldsymbol{q}_T + 6.8\boldsymbol{b}^*/b^*| \leqslant 3.4\,nm^{-1}$ for B and $|\boldsymbol{q}_T - 6.8\boldsymbol{c}^*/c^*| \leqslant 3.4\,nm^{-1}$ for C. The EELS spectra (vii) and (viii) in Fig. 5(c) acquired, respectively, from areas B and C exhibit similar features (as denoted by solid squares and triangles) to $q_{TC} = 0.84$ (mainly characterized by $1s \rightarrow 2p_{xy}$ excitation) and $0\,nm^{-1}$ (characterized by $1s \rightarrow 2p_z$ excitation) in Fig. 1. It is noteworthy that the contribution of $1s \rightarrow 2p_{xy}$ excitation in EELS intensity increases when the range of $\boldsymbol{q}_T$ is reduced for [100] because of $q_L \| (2\boldsymbol{a}^* - \boldsymbol{b}^*)$, as shown in spectrum (vi) acquired from $|\boldsymbol{q}_T| \leqslant 3.4\,nm^{-1}$ [shown as dotted circle A in Fig. 5(b)], where the intensity at 61.4 eV in spectrum (vi) is greater than that in spectrum (v).

D. Considering Li *K* edge anisotropy for the quantification of Li contents

We briefly discuss consideration of the Li *K* edge anisotropy for quantitative evaluation of x in Li_xCoO_2 using two approaches: The first is a standard approach using the partial scattering cross section (PSCS) [24]. The second is an empirical approach using the EELS intensity at 61.4 eV [6]. When we specifically examine the Li_xCoO_2 electrode materials for lithium ion batteries, x should be estimated as the molar ratio of Li/Co because oxide ions can be extracted at the surfaces of Li_xCoO_2 particles [6]. The range of $\boldsymbol{q}_T$ used in conventional TEM-EELS is described as $|\boldsymbol{q}_T| \leqslant q_\beta$, where q_β is the collection radius of scattered electrons. The results presented in Sec. III A–C demonstrate that the spectrum features of the Li *K* edge for Li_xCoO_2 ($x = 1$) depend on both $|\boldsymbol{q}_T|$ and the crystallographic orientation. These dependences are expected to exist for Li_xCoO_2 ($0.25 \leqslant x < 1$) with anisotropic structures [34]. The first approach for quantification of x in EELS requires the integrated intensity for the Li *K* edge, $I_{Li\ K}$ and the calculated PSCS for the Li *K* edge, $\sigma_{Li\,K}$ in an energy range, simultaneously requiring those of either Co $M_{2,3}$ or Co $L_{2,3}$ edges [24]. However, the extraction of Li *K* edge from an EELS spectrum (i.e., Li *K* and Co $M_{2,3}$ edges combined with polarization) is difficult. An alternative method is the extraction of the superposition of Li *K* and Co $M_{2,3}$ edges, $I_{Li\,K+Co\,M_{2,3}}$ without separating their edges and the additional use of Co $L_{2,3}$ edge, $I_{Co\,L_{2,3}}$ measured using conditions equivalent to those for Li *K* and Co $M_{2,3}$ edges. The Li/Co ratio x is given as

$$x = (I_{Li\,K+Co\,M_{2,3}}/I_{Co\,L_{2,3}})(\sigma_{Co\,L_{2,3}}/\sigma_{Li\,K})\text{-}\sigma_{Co\,M_{2,3}}/\sigma_{Li\,K}, \quad (2)$$

where $\sigma_{Co\,M_{2,3}}$ and $\sigma_{Co\,L_{2,3}}$, respectively, represent the calculated PSCS for Co $M_{2,3}$ and $L_{2,3}$ edges (Sec. F in Supplemental Material [22]). Consideration of the anisotropy of core-loss edges, especially Li *K* edge, is necessary for the calculations of PSCS in Eq. (2). Small values of q_β ($<1\,nm^{-1}$) and the energy range for integration, Δ (<10 eV) reduces the accuracy of x unless the calculated PSCS is precise because $I_{Li\,K+Co\,M_{2,3}}$ and $\sigma_{Li\,K}$ can vary considerably with small changes in q_β (Fig. S5 [22]). Presumably, choosing $5 \leqslant q_\beta \leqslant 10\,nm^{-1}$ and $\Delta \geqslant 30$ eV (wholly covering Li *K*, Co $M_{2,3}$, or Co $L_{2,3}$ edges) is adequate for practical TEM-EELS analyses, although

evaluation of the accuracy of x using Eq. (2) is left as a subject for future work. The second approach for quantifying x uses the dependence of a variable parameter, i.e., an area ratio of S_A/S_B defined for the 61.4-eV peak on x [6]. Both q_β and crystallographic orientation strongly affect the intensity at 61.4 eV. Therefore, we presume that the uses of a specific value of q_β ($\geqslant 5\,\mathrm{nm}^{-1}$) and the [001] electron incident direction are acceptable for obtaining better accuracy of x. For both approaches, considerations of the anisotropy of Li K edge are important for improving the accuracy of x. Observation of the inhomogeneous distribution of Li ions using more accurate x in a Li_xCoO_2 particle during electrochemical cycling will be beneficial for clarifying the electrode degradation mechanism.

IV. CONCLUSION

In summary, important differences were found in electron excitation between $1s \rightarrow 2p_{xy}$ and $1s \rightarrow 2p_z$ for Li in $LiCoO_2$ using $\boldsymbol{q}$-dependent EELS and first-principles calculation. We also demonstrated that these differences cause crystallographic orientation dependence of the Li K edge. Consideration of the scattering vector and crystallographic orientation in EELS measurement of Li K edge for lithiated transition-metal oxides with layered structures is indispensable for quantification of the Li contents and identification of atomic site of Li more accurately to clarify the degradation mechanisms of the electrode materials during electrochemical cycling.

ACKNOWLEDGMENTS

J.K. appreciates the sample preparation assistance of H. Sakurai (NIMS). This work was partly supported by JSPS KAKENHI Grants No. JP16K13690 and No. JP16H05965. T.M. is supported by the Mitsubishi Science Foundation (Grant No. 27143) and Grants-in-Aid for Scientific Research from MEXT (Grants No. 25106003 and No. 26249092).

[1] T. Ohzuku and A. Ueda, J. Electrochem. Soc. **141**, 2972 (1994).
[2] T. Mizokawa, Y. Wakisaka, T. Sudayama, C. Iwai, K. Miyoshi, J. Takeuchi, H. Wadati, D. G. Hawthorn, T. Z. Regier, and G. A. Sawatzky, Phys. Rev. Lett. **111**, 056404 (2013).
[3] J. Kikkawa, T. Akita, M. Tabuchi, M. Shikano, K. Tatsumi, and M. Kohyama, Electrochem. Solid-State Lett. **11**, A183 (2008).
[4] F. Wang, J. Graetz, M. S. Moreno, C. Ma, L. J. Wu, V. Volkov, and Y. M. Zhu, ACS Nano **5**, 1190 (2011).
[5] N. Taguchi, T. Akita, H. Sakaebe, K. Tatsumi, and Z. Ogumi, J. Electrochem. Soc. **160**, A2293 (2013).
[6] J. Kikkawa, S. Terada, A. Gunji, T. Nagai, K. Kurashima, and K. Kimoto, J. Phys. Chem. C **119**, 15823 (2015).
[7] K. Zeppenfeld, Phys. Lett. A **25**, 335 (1967).
[8] R. D. Leapman and J. Silcox, Phys. Rev. Lett. **42**, 1361 (1979).
[9] G. A. Botton, J. Electron. Spectrosc. Relat. Phenom. **143**, 129 (2005).
[10] F. C. Brown, R. Z. Bachrach, and M. Skibowski, Phys. Rev. B **13**, 2633 (1976).
[11] R. D. Leapman, P. L. Fejes, and J. Silcox, Phys. Rev. B **28**, 2361 (1983).
[12] S. M. Heald and E. A. Stern, Phys. Rev. B **16**, 5549 (1977).
[13] M. H. Krisch, F. Sette, C. Masciovecchio, and R. Verbeni, Phys. Rev. Lett. **78**, 2843 (1997).
[14] T. T. Fister, M. Schmidt, P. Fenter, C. S. Johnson, M. D. Slater, M. K. Chan, and E. L. Shirley, J. Chem. Phys. **135**, 224513 (2011).
[15] V. Mauchamp, F. Boucher, G. Ouvrard, and P. Moreau, Phys. Rev. B **74**, 115106 (2006).
[16] N. Wiser, Phys. Rev. **129**, 62 (1963).
[17] N. Vast, L. Reining, V. Olevano, P. Schattschneider, and B. Jouffrey, Phys. Rev. Lett. **88**, 037601 (2002).
[18] P. Moreau and F. Boucher, Micron **43**, 16 (2012).
[19] E. L. Shirley, Phys. Rev. Lett. **80**, 794 (1998).
[20] T. Mizoguchi, W. Olovsson, H. Ikeno, and I. Tanaka, Micron **41**, 695 (2010).
[21] H. Sakurai, S. Takenouchi, N. Tsujii, and E. Takayama-Muromachi, J. Phys. Soc. Jpn. **73**, 2081 (2004).
[22] See Supplemental Material at http://link.aps.org/supplemental/10.1103/PhysRevB.98.075103 for structure of $Na_{0.72}CoO_2$, local field effects, raw spectra of the q-dependent EELS, Co $M_{2,3}$ edges, integrated q-dependent EELS, and Eq. (2).
[23] P. A. Midgley, Ultramicroscopy **76**, 91 (1999).
[24] R. F. Egerton, *Electron Energy-loss Spectroscopy in the Electron Microscope*, 3rd ed. (Springer, New York, 2011).
[25] K. Zeppenfeld, Opt. Commun. **1**, 119 (1969).
[26] N. D. Browning, J. Yuan, and L. M. Brown, Ultramicroscopy **38**, 291 (1991).
[27] G. Andris, K. Stefan, M. Christian, N. Dmitrii, P. Pasquale, R. Santiago, S. Stephan, W. Ute, and D. Claudia, J. Phys.: Condens. Matter **26**, 363202 (2014); The exciting Code. http://exciting-code.org/.
[28] J. P. Perdew, K. Burke, and M. Ernzerhof, Phys. Rev. Lett. **77**, 3865 (1996).
[29] J. K. Dewhurst, S. Sharma, L. Nordstrom, F. Cricchio, O. Granas, and E. K. U. Gross, The Elk Code Manual, ver. 4.3.6.; Elk FP-LAPW Code. http://elk.sourceforge.net/.
[30] G. Onida, L. Reining, and A. Rubio, Rev. Mod. Phys. **74**, 601 (2002).
[31] W. Olovsson, I. Tanaka, T. Mizoguchi, G. Radtke, P. Puschnig, and C. Ambrosch-Draxl, Phys. Rev. B **83**, 195206 (2011).
[32] H. W. Zandbergen, M. Foo, Q. Xu, V. Kumar, and R. J. Cava, Phys. Rev. B **70**, 024101 (2004).
[33] H. J. Lin, Y. Y. Chin, Z. Hu, G. J. Shu, F. C. Chou, H. Ohta, K. Yoshimura, S. Hebert, A. Maignan, A. Tanaka, L. H. Tjeng, and C. T. Chen, Phys. Rev. B **81**, 115138 (2010).
[34] H. Ben Yahia, M. Shikano, and H. Kobayashi, Chem. Mater. **25**, 3687 (2013).